

TOPICAL REVIEW • OPEN ACCESS

In-situ measurement methods for microscale surface impurities in powder bed fusion: a review

To cite this article: Ahmet Koca *et al* 2025 *Meas. Sci. Technol.* **36** 012001

View the [article online](#) for updates and enhancements.

You may also like

- [A tracer-free photographic method for the estimation of the velocity field in a liquid metal pool](#)

Jad Houssein, Gaëtan Le Goïc, Mickaël Courtois et al.

- [A point cloud segmentation algorithm based on multi-feature training and weighted random forest](#)

Fuqun Zhao, He Huang, Nana Xiao et al.

- [Adaptive IMU error correction algorithm for dual-antenna GNSS/IMU integrated vehicle attitude determination](#)

Lei Jiang, Rui Sun, Qi Cheng et al.

Topical Review

In-situ measurement methods for microscale surface impurities in powder bed fusion: a review

Ahmet Koca^{1,*} , Helia Hooshmand¹, Richard Leach¹ and Mingyu Liu^{1,2,*} ¹ Manufacturing Metrology Team, Faculty of Engineering, University of Nottingham, Nottingham NG8 1BB, United Kingdom² School of Engineering, University of Lincoln, Lincoln LN6 7TS, United KingdomE-mail: ahmet.koca@nottingham.ac.uk, SaLiu@lincoln.ac.uk and Samuel.Liu@nottingham.ac.uk

Received 29 May 2024, revised 23 August 2024

Accepted for publication 2 October 2024

Published 14 October 2024



CrossMark

Abstract

Despite ongoing improvements and optimisation efforts, the powder bed fusion (PBF) process continues to face challenges related to repeatability, robustness, and stability. These challenges can lead to the formation of microscale surface impurities on each layer, such as balling, spatter and surface pores, which can adversely affect the overall quality of the final part. The layer-by-layer fabrication approach in PBF offers an opportunity to assess fabrication quality in real-time by detecting these impurities at each layer during the manufacturing process through *in-situ* sensing methods. With advancements in sensing and computing technologies, there has been a significant increase in studies focused on developing *in-situ* methods for the real-time detection of surface impurities and feedback mechanisms. However, it is necessary to understand the effectiveness and capability of these *in-situ* methods in detecting microscale surface impurities, as well as to evaluate their potential advantages, drawbacks, and the existing gaps in the literature. This study first summarises the common microscale surface impurities and their potential impacts on part quality, including mechanical properties and surface finish. It then reviews the existing *in-situ* methods capable of detecting these microscale impurities, providing insights into the strengths and limitations of current techniques, and identifying gaps in the literature while suggesting directions for future research.

Keywords: powder bed fusion, *in-situ* measurement, surface impurities, defect detection

* Authors to whom any correspondence should be addressed.



Original content from this work may be used under the terms of the [Creative Commons Attribution 4.0 licence](https://creativecommons.org/licenses/by/4.0/). Any further distribution of this work must maintain attribution to the author(s) and the title of the work, journal citation and DOI.

1. Introduction

Additive manufacturing (AM) is a rapidly growing fabrication method that can produce complex geometries by adding/fusing material layer-by-layer according to the three-dimensional (3D) models of the parts [1]. Although the origins of AM date back to the 1860s, the first commercial AM machine was introduced by 3D Systems in 1987 [2]. The pace of development significantly accelerated with advancements in computer technology and the introduction of powerful graphical interfaces. According to the Wohlers Report 2024 [3], sales of metal AM systems have steadily increased since 2002 (figure 1), growing by more than 700% over the past decade.

AM offers a significant advantage over traditional fabrication methods in terms of design freedom. AM parts can be designed without considering the tools and fixtures required for conventional manufacturing. This feature allows for parts with complex geometries and features that are difficult or impossible to fabricate using traditional methods [4]. Additionally, time and cost savings can be achieved by minimising the need for various fabrication processes and the accompanying fixturing requirements. However, in order to fabricate an AM part with the desired quality, an understanding of the underlying processes, materials, and their limitations is required. Despite improvements and optimisation studies in AM, defects still occur due to the lack of fabrication stability, robustness and repeatability of the manufacturing processes [5–7]. As such, it is essential to detect and analyse defects to inspect and monitor the fabrication quality of components.

Powder bed fusion (PBF) is the most widely used mature metal AM technique [8]. It uses a laser (laser-based PBF, PBF-LB) or electron beam (electron-based PBF, PBF-EB) to melt and fuse powder layers to fabricate 3D parts. During the fabrication process, microscale surface impurities (smaller than 1 mm), such as balling [9], spatter [10] and surface pores [11], may form on layer surfaces. These impurities can significantly compromise the integrity of the part by diminishing its quality. In this paper, ‘part quality’ refers to the properties of the fabricated parts, including their mechanical, thermal, and dynamic characteristics, as well as the quality of their surface finish. Several studies have demonstrated that surface impurities can reduce mechanical properties such as strength [12], microhardness [13] and fatigue life [14]. Moreover, they play a critical role in crack initiation [15].

Surface impurities can be the source of other defects and further negatively impact the part quality [16, 17]. For instance, Gu and Shen [9] investigated that the amount of partially melted particles increases the formation of lack of fusion (LOF). Zhang *et al* [18] presented a positive correlation between surface impurities and internal porosities. Sanviemvongsak *et al* [19] suggested that surface impurities can cause oxidation. Romano *et al* [20] observed that surface cracks, exacerbated by impurities, decrease fatigue resistance and Zhu *et al* [21] explored a correlation between surface texture and porosity. In other words, the presence of surface impurities not only indicates poor surface quality but can also be a sign of overall poor part quality [16–20]. As a result, the

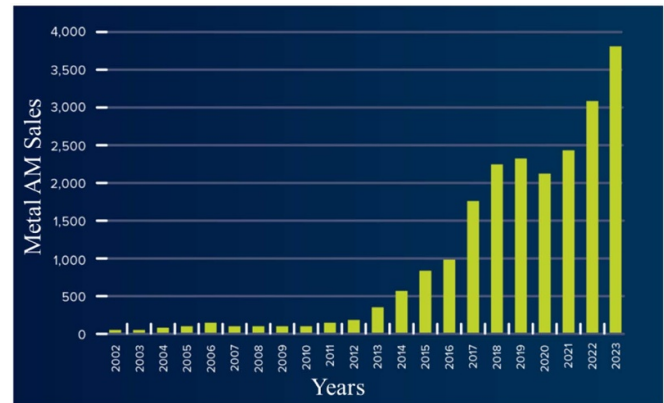


Figure 1. Metal AM sales between 2002–2023, Wohlers Report 2024 [3].

scope of this paper focuses on microscale surface impurities in PBF.

Microscale surface impurities in PBF can be measured after the fabrication using high-resolution *ex-situ* methods such as x-ray computed tomography (XCT) [22, 23], optical methods, such as coherence scanning interferometry [24, 25], confocal microscopy (CM) [24–27] and focus variation [25, 28]. In *ex-situ* methods, the part may need to be transported from a manufacturing site to a metrology site, which involves significant delays and potential harm by sample degradation or contamination. It should be noted that most of these surface topography measuring techniques, though having high resolution, can be relatively costly.

On the other hand, the layer-by-layer fabrication method enables *in-situ* monitoring of surface impurities on each layer during the fabrication process [29–31], which is valuable because it allows for real-time data collection and analysis to help identify defects. It can also enable closed-loop feedback control to correct defects during their formation.

Some of the earliest research on *in-situ* monitoring was conducted in 1994 by Melvin *et al* [32] and Benda [33]. Melvin *et al* [32] utilised video microscopy to gain insights into the behaviour of powder during fabrication, while Benda [33] was the first to measure melt pool temperature using an *in-situ* infrared (IR) sensor. These pioneering studies marked the beginning of using *in-situ* sensors for analysing PBF fabrication. Following these initial studies, researchers increasingly focused on *in-situ* methods, primarily based on visible and thermal sensing [34]. Particularly after 2010, there was a growing interest in the defect detection capabilities of *in-situ* methods. One of the first defect detection methods using *in-situ* sensing was proposed by Berument *et al* [35], who concentrated on detecting issues related to powder coating, such as insufficient or excessive powder layering. With advancements in sensor technology and machine learning (ML) algorithms, research in defect detection has expanded significantly. Figure 2 shows the number of papers published on *in-situ* measurement and monitoring methods for PBF since 1994 according to the Scopus database, highlighting the rapid growth of interest in this area.

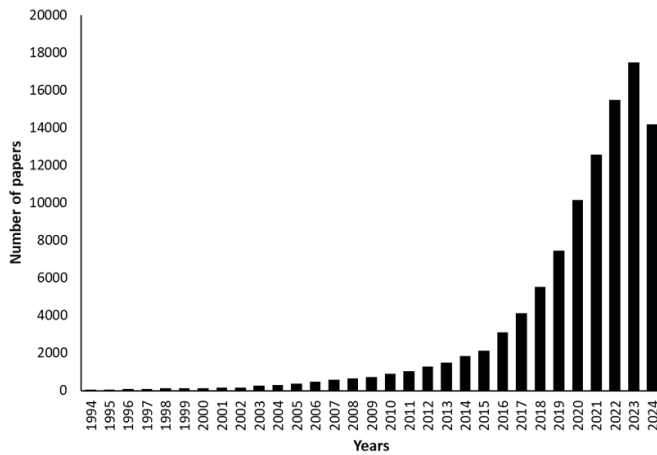


Figure 2. The number of published papers about *in-situ* methods on PBF based on the Scopus database.

Microscale surface impurities need to be detected in real-time using *in-situ* methods to evaluate fabrication quality or to correct these impurities during fabrication through real-time feedback control. Several recent review papers have examined *in-situ* measurement and monitoring methods in PBF [5, 30, 36]. However, our review paper offers a unique contribution by focusing on the most recent *in-situ* methods specifically designed to detect microscale surface impurities. The paper also critically evaluates the capabilities and limitations of each method, emphasising detection accuracy and the range of detectable impurity sizes. It begins by introducing common microscale surface impurities, discussing their potential formation mechanisms, and assessing their impact on the final quality of manufactured parts. Finally, the paper summarizes key findings related to these methods, highlighting their advantages and limitations, and identifies gaps in the current literature, offering suggestions for future research directions.

2. Microscale surface impurities

The surface quality of each layer in PBF fabrication can play a crucial role in determining a part's overall performance [21], which is due to the layerwise fabrication process, where the quality of each layer can influence the subsequent layers' quality. Microscale surface impurities refer to protrusions or recesses, such as balling, spatter and pores found on a surface. These impurities can decrease the quality of the fabricated parts. In the literature, several studies have demonstrated a direct correlation between these impurities and part quality [11, 37–41]. Furthermore, other studies have indicated an indirect correlation, as these impurities can contribute to forming other defects such as internal pores, LOF and cracks, further impacting the overall part quality [10, 42–47].

This section focuses on common microscale surface impurities, protrusions and recesses that can arise during fabrication, their influence on part quality, and the correlations between these impurities and other defects. Understanding and

managing these impurities is vital to ensuring the overall performance and reliability of PBF-fabricated parts.

2.1. Balling

Balling is one typical fabrication defect encountered in PBF, which is formed by breaking the molten metal into droplets in the shape of separate beads (see figure 3(a)) [48]. This phenomenon arises during the process of powder melting, wherein the weld track experiences a reduction in surface energy due to surface tension often resulting from inadequate wettability and non-optimal process parameters [49, 50]. Balling has been categorised based on its shape and dimensions into ellipsoidal and spherical forms, with reported dimensions ranging from approximately 3–500 μm [9, 50, 51].

The balling phenomenon causes the interaction between the laser beam and the surface to become unstable, leading to the formation of irregular weld tracks. These irregular weld tracks lead to insufficient bonding between layers, resulting in phenomena such as rough surfaces [53–57], porosity [42–44] and reduced part density [51, 58, 59].

2.2. Spatter

Spatter, a common occurrence in PBF (see figure 3(b)), is generally undesirable in many applications due to its adverse effects on part quality [10, 39, 60, 61]. It is a by-product of the PBF process, resulting from material ejection from the melt pool due to a combination of physical phenomena, including vapour pressure, laser-induced plasma and gas flow [62–64]. Notably, spatter particles typically exhibit larger sizes compared to virgin powder particles, consequently requiring higher energy to melt [39].

The size of spatters depends on the powder used in the fabrication process. The smallest spatters can be as small as the smallest powder particles, while the largest spatters can be up to ten times larger than the average powder size. Ali *et al* [45] observed that the size of spatters in D10 and D50 was similar to that of virgin powder, approximately 30 μm and 45 μm , respectively. Additionally, Liu *et al* [38] reported spatters measuring around 400 μm , which is about ten times larger than the average powder size of 42.83 μm .

Spatters can induce high surface irregularities [65], leading to incomplete fusion between layers [37, 38]. As a consequence, defects such as internal pores [10, 45, 46] and LOF [47] can form. Spatters and other potential defects caused by spatters can lead to fatigue strength degradation, reduced part density and poor tensile strength [37–39]. Furthermore, large spatter particles attached to the layer surface can be removed by the recoater during subsequent layering, leaving pits behind and potentially compromising the recoating mechanism [46].

2.3. Surface pores

The surface pore is another type of impurity that occurs as dents, craters or cave-like open pores (see figure 3(b)) on the surface of PBF parts [40, 66]. Several hypotheses have been

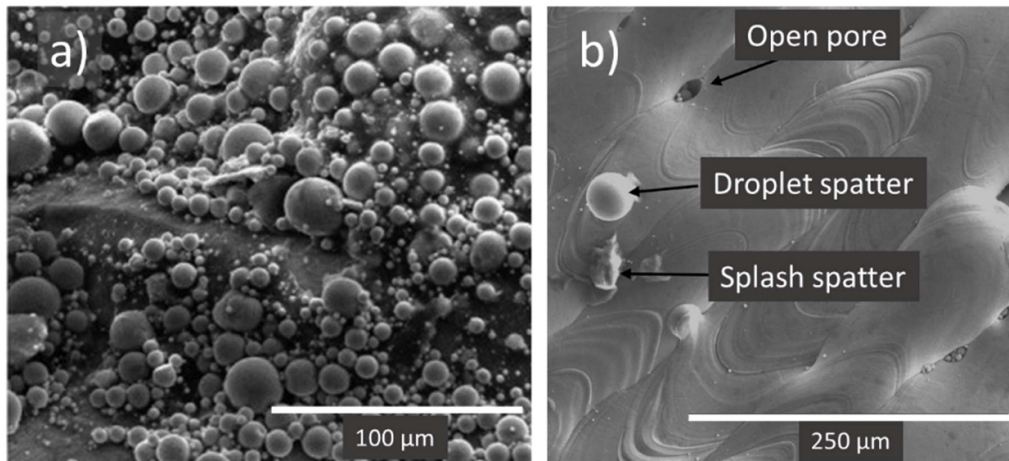


Figure 3. (a) SEM image showing balling characteristics [9], (b) surface impurities [52].

proposed regarding the formation mechanism of the surface pores, focusing on the emergence of pores on the layer surface and insufficient liquid feeding [40, 67, 68]. Empirical studies indicate that non-optimal process parameters, such as high scanning speeds and large hatch distances, contribute to the increased occurrence of surface pores [40, 69–72].

Surface pores have a notable association with internal pores, leading to diminished part density and compromising the mechanical performance of the parts [11, 40, 41, 73]. Furthermore, the presence of surface pores escalates surface roughness and can act as initiation points for crack defects [11, 69, 72, 74]. Some studies have noted the presence of pores on the fractured surfaces or within product sizes ranging from 2 μm to 10 μm. These studies have proposed that these pores may be possible sources of reduced part quality [42, 43].

Overall, microscale surface impurities in PBF could impact the overall fabrication quality, necessitating their measurement and assessment in the context of fabrication quality control.

3. *In-situ* measurement methods

Layerwise fabrication in PBF enables the implementation of *in-situ* measurement techniques during the manufacturing process [36]. *In-situ* measurement methods involve using sensors to collect data about process stability and product quality directly from where the process is taking place. Employing *in-situ* measurement techniques in PBF makes it feasible to detect and analyse surface impurities that may form on each layer.

The occurrence of impurities at any layer can significantly impact the quality of subsequent layers, consequently affecting the final part's overall quality [41, 60]. *In-situ* measurement methods can provide the means to identify impurities formed on each layer. Although certain defects, such as shrinkage and distortion, may not be directly observable through *in-situ* measurements, anomalies associated with these defects can be detected. By enabling real-time defect detection, it

becomes possible to prevent/decrease the formation of subsequent defects through active control of process parameters [75].

In certain instances, *in-situ* measurements may not provide a straightforward depiction of surface impurities, particularly when dealing with data that could be more intuitively interpretable, such as acoustic signals [76]. In such scenarios, surface impurities can still be detected using correlations between the non-interpretable *in-situ* data and interpretable *ex-situ* data [76–78].

In the following section, we present and examine various *in-situ* measurement methods that specifically target the detection and characterisation of microscale surface impurities.

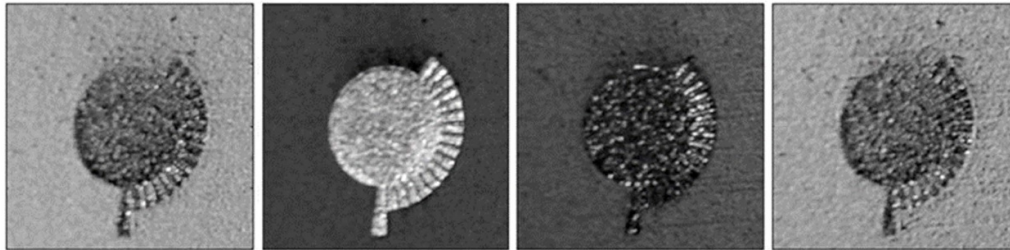
3.1. Visible sensing

Visible range sensors can capture images of the powder bed or melt tracks continuously during the fabrication or a small number of times after melting and/or after the deposition of a new layer [79, 80]. In order to enable *in-situ* measurement, the camera vision system must have sufficient speed so as not to disrupt the ongoing fabrication process. Seminal studies have shown that visible imaging systems have the potential to detect powder bed irregularities [81, 82]. Currently, visible imaging systems find applications in industrial PBF machinery for *in-situ* process quality measurement [30]. Table 1 shows *in-situ* measurement methods using visible range imaging with their specifications.

In visible images, surface impurities exhibit a distinctive contrast compared to the regular surface. In order to accurately identify surface impurities from the images recorded by visible range cameras, accurate segmentation and contour identification are essential [79, 86, 89]. The accuracy of detection and the minimum detectable size of surface impurities depend not only on the spatial resolution but also on the illumination of the vision system, as the interaction between the layer surface and lighting may give rise to undesirable reflections [90, 91]. The effect of different lighting on the images can be seen in figure 4.

Table 1. *In-situ* measurement methods using visible range imaging for PBF.

References	Sensor	Resolution	Detectable features/Size range	Detection method/algorithm	Detection Accuracy
[83]	Monochrome CCD Camera	Spatial resolution: $\sim 30 \mu\text{m}/\text{pixel}$	$>90 \mu\text{m}$	Image processing	Not specified
[84]	DSLR Camera	Spatial resolution: $10\text{--}13 \mu\text{m}/\text{pixel}$	$\sim 500 \mu\text{m}$	Image processing	Not specified
[85]	DSLR Camera	Spatial resolution: $\sim 62.5 \mu\text{m}/\text{pixel}$	$\geq 40 \mu\text{m}$	Convolutional neural network	Depends on the size: less than 50% for $\sim 40 \mu\text{m}$, around 90% for $\sim 200 \mu\text{m}$, and 100% for larger than $475 \mu\text{m}$ $\sim 87\%$
[86]	DSLR Camera	Pixel size range: $45 \times 47 \mu\text{m}$ – $67 \times 88 \mu\text{m}$	$50\text{--}750 \mu\text{m}$	Image processing	
[87]	Monochrome CCD Camera	Not specified	$\geq 10 \mu$	Particle analysis	Not specified
[88]	Line Camera	Spatial resolution: $5.97 \mu\text{m}/\text{pixel}$	$\geq 12.4 \mu\text{m}$	Feature-based analysis	Not specified

**Figure 4.** (a) Powder bed images using different lighting conditions [90].

Micro-scale protrusions on the PBF surface can be detected using the contrast between the elevated area and raw powder in surface images taken after the powder deposition process [92]. Zur Jacobsmuhlen *et al* investigated [83] the detection of the elevated areas on PBF surfaces by using a monochrome CCD camera to record surface images having a spatial resolution of approximately $30 \mu\text{m}/\text{pixel}$. While disregarding small regions measuring $90 \mu\text{m}$ in diameter, it has been indicated that their method yields a minimum resolvable detail of approximately $50 \mu\text{m}$ in size for a field of view measuring $180 \times 120 \text{mm}$.

In some studies, XCT is used as ‘ground truth’ data to validate their findings or correlate them with *in-situ* data. Lu *et al* [84] designed a vision setup with a digital single-lens reflex (DSLR) camera and LED light sources, in which intensity values were employed for detecting surface irregularities (see figures 5(a) and (b)), and the results were validated using XCT data. This method can detect holes with a minimum diameter of $500 \mu\text{m}$ and squares with a minimum length of $500 \mu\text{m}$.

Snow *et al* [85] employed a ML algorithm to detect defects from *in-situ* layer images, utilising *ex-situ* XCT data as labelled defects for training. They attained more than 85% accuracy in defect detection for defects larger than $200 \mu\text{m}$, both within the same dataset and with unseen data. Additionally, the study compared spatters detected through *in-situ* measurements and LOF identified via *ex-situ* XCT analysis. Notably, they presented a significant correlation between spatters and LOF defects smaller than $500 \mu\text{m}$.

Designing synthetic defects has been proposed as a way of evaluating the system’s defect detection performance. Abdelrahman *et al* [86] developed a defect detection algorithm using surface images of parts with intentional defects. They demonstrated around 87% detection accuracy with the targeted defect size ranging from $50 \mu\text{m}$ to $750 \mu\text{m}$.

Modaresialam *et al* [87] showed that *in-situ* visible imaging can be used for real-time defect detection. They developed an algorithm using LabView software to halt fabrication when

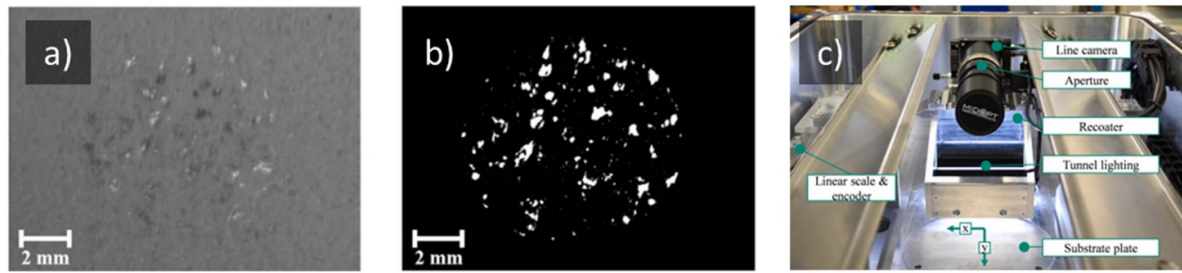


Figure 5. (a) Optical image captured during printing, (b) binarized image after processing [84], and (c) dynamic monitoring system [88].

Table 2. *In-situ* measurement methods using thermal sensing for PBF.

References	Sensor	Detectable features/ Size range	Detection method/ algorithm	Detection Accuracy
[104]	NIR range imaging	$> \sim 200 \mu\text{m}$	Image processing	79%
[102]	IR range imaging	$0.1 \times 10^6 - 2.0 \times 10^6 \mu\text{m}^2$	Image analysis software (MIPAR)	Not specified
[99]	NIR range imaging	$> 100 \mu\text{m}$	Image processing	Not specified
[103]	IR range imaging	$600 - 900 \mu\text{m}$	Image processing	100%
[96]	IR range imaging	$> \sim 300 \mu\text{m}$	Manual analysis (by looking at the graphs)	Not specified
[105]	NIR range imaging	$150 \mu\text{m}$ (can detect smaller features with low accuracy)	A specific algorithm to correlate the OT and x-ray tomography data	90/95% (probability of detection)
[101]	IR range imaging	$50 - 500 \mu\text{m}$	Image processing	Depends on the size: less than 50% for $< 50 \mu\text{m}$, 100% for $> 500 \mu\text{m}$
[100]	IR range imaging	$750 \mu\text{m}$	Image processing	Not specified

critical defects were detected. The method includes a visible range camera with a resolution of 1696×1710 pixels and can detect microcracks and porosities as small as $10 \mu\text{m}$.

The above imaging systems were all in fixed positions. Fischer *et al* [88] implemented a dynamic image-capturing approach to address the limitation of fixed positioning. They mounted a line camera on the recoater of a PBF machine (see figure 5(c)) to capture powder bed images during powder deposition, obtaining images with a width of 97.67 mm and a lateral resolution of $5.97 \mu\text{m}/\text{pixel}$. This setup allowed them to identify features such as spatter, balling and unmelted powder with a minimum size of $12.4 \mu\text{m}$.

3.2. Thermal sensing

In the manufacturing process, defects may arise due to thermal inhomogeneity [93] or, conversely, may lead to thermal inhomogeneity [94]. Consequently, thermal data can be harnessed to detect defects by identifying thermal inhomogeneities, offering valuable insights into process quality. Furthermore, thermal data has been previously utilised to predict the internal microstructure of parts [95].

During the PBF process, *in-situ* thermal information about layer surfaces or melt tracks can be collected using sensors operating in the IR or near-IR (NIR) range (see an example implementation in figure 6(a)) [96–105], which can be achieved through continuously recording images of layers using high-frame-rate sensors [100]. However, continuous recording presents challenges, such as generating substantial amounts of data and being sensitive to metallisation when employing sensors [95]. One approach to mitigate the impact of these challenges is to opt for single-image recording for each layer using a mechanical shutter or placing the sensor outside the building chamber [98]. However, capturing a single image delays temperature information, as the scanning process takes time, and recording data from outside the chamber necessitates coordinate transformation. Table 2 summarises *in-situ* measurement methods using thermal sensing along with their specifications.

Some *in-situ* thermal sensing methods focused on detecting spatters and demonstrated their impact on process quality. For instance, Schwerz *et al* [98] focused on the detection of spatters using long-exposure NIR range imaging of the layer surface (see figure 6(b)). The spatters were examined using scanning electron microscopy (SEM) and exhibited a

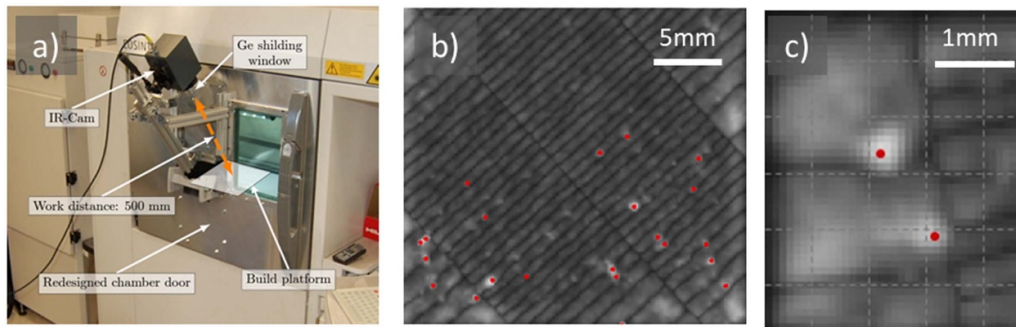


Figure 6. (a) *In-situ* temperature measurement setup [96], (b) spatter detection from a thermal image in [98], (c) and in [104].

bimodal size distribution, with peaks at 30 μm and 90 μm , and the largest size measured approximately 200 μm . They conducted an *ex-situ* ultrasonic inspection to validate the findings and observed LOF in areas where the spatters were redeposited. Afterwards, Schwerz *et al* [104] used an embedded *in-situ* monitoring system (EOSTATE exposure optical tomography) which included a three-megapixel sCMOS camera with a 900 nm bandpass filter for spatter detection. An image processing algorithm was employed to detect bright regions indicative of spatter defects (see figure 6(c)). A correlation was observed between the spatters detected using the OT system and LOF defects detected through XCT. However, a slight offset between the two detection systems was noted, potentially attributed to spatters causing LOF in subsequent layers.

Yakout *et al* [102] also investigated spatter detection using an *in-situ* high-speed IR thermography system. In this study, the size, shape and distribution of the spatters were analysed, and the correlation between these features and the processing conditions was investigated. The sensor was positioned outside the chamber, and data was recorded through a protected window to ensure the sensor's safety in the harsh environment.

Another focus in *in-situ* thermal sensing is detecting porosity defects. Nandwana *et al* [99] studied porosity detection from NIR images captured immediately after the melting process using image processing techniques. They used variations in surface emissivity to detect pores larger than 100 μm . Furthermore, a correlation was established between the outcomes of fatigue performance testing and the results of pore detection. Notably, failures were observed to coincide with the regions where the most prominent pores were identified. Yoder *et al* [97] utilised the same experimental setup to explore the connection between *in-situ* thermal data and the mechanical performance of topology-optimised parts. The study demonstrated a correlation between pores detected from *in-situ* data and premature failure in a sample.

Real-time defect detection makes controlled fabrication possible by changing process parameters or stopping the fabrication. Mireles *et al* [103] presented a closed-loop automatic feedback control for PBF-EB by integrating an IR camera into a PBF-EB machine. An algorithm was developed to automatically detect porosity by processing the IR images recorded during the process. The algorithm achieved a 100% detection rate of the artificially made porosity defects ranging from

600 μm to 900 μm in size on the cylindrical parts. Krauss *et al* [96] designed artificial defects in parts by creating holes of different sizes to simulate gas pores and cracks. An IR camera with a lateral resolution of 250 $\mu\text{m}/\text{pixel}$ was employed for *in-situ* thermal sensing of the powder bed. The thermal diffusivity data showed that the minimum detectable defect size is approximately 300 μm . Additionally, the correlation between the formation of ejected particles and the thermal distribution was investigated.

Several studies have explored the detection of LOF defects using *in-situ* thermal sensing methods. For instance, Bamberg *et al* [105] utilised an sCMOS camera with a NIR filter. Their system was capable of capturing images with extended exposure times. This approach demonstrated the capacity to detect LOF as small as 150 μm in size, yielding a probability of detection (POD) of 90/95%. The system's capability to detect smaller defects was enhanced, albeit with a slightly reduced POD. In another investigation conducted by Bartlett *et al* [101], an IR camera sensitive to long-wave IR wavelengths was positioned externally to the PBF machine. This setup facilitated the capture of relative temperature distributions across the printed layer. Through the analysis of IR images, LOF with diameters below 50 μm were detected with a success rate of 50%. Additionally, defects exceeding 500 μm exhibited a 100% detection success rate.

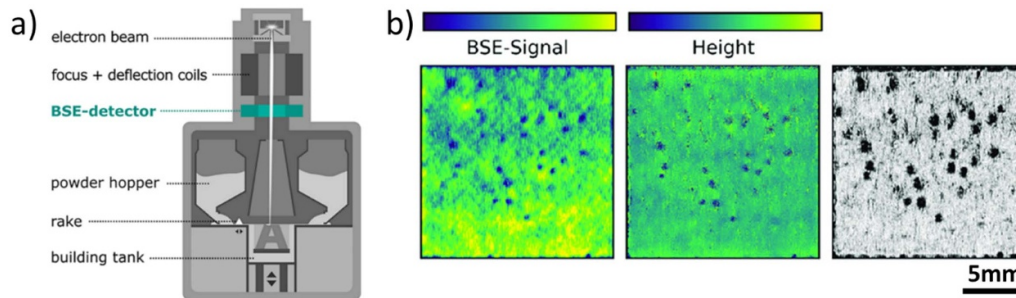
Mahmoudi *et al* [100] investigated the detection of cavity defects from *in-situ* thermal data of the melt pool. They used high-speed sensors to collect *in-situ* thermal information. Their study demonstrated that their method successfully detected defects of 750 μm in size.

3.3. Electronic imaging

Electronic imaging, also called electron optical (ELO) imaging, operates on the same fundamental principle as traditional SEM [106]. In this technique (see an example of an integrated system in figure 7(a)), a detector captures backscattered or secondary electrons resulting from the interaction between the process beam and the powder material [107]. The intensity of the collected signal is influenced by both the current of the electron beam and the atomic number of the material [106–108]. Notably, the surface topography is

Table 3. *In-situ* measurement methods based on ELO for PBF.

References	Sensor	Detectable features/ Size range	Detection method/algorithm
[109]	BSE sensor	~300 μm	Based on the correlation between ELO images, optical images, and surface topography data
[110]	BSE sensor	100–200 μm	Based on the correlation between ELO images and optical images
[111]	BSE sensor	>~100 μm	Image processing (contour identification, edge detection)

**Figure 7.** (a) Schematic diagram of a PBF-EB with a BSE detector installed [106], (b) Surfaces of powder-bed samples taken by the *in-situ* ELO method (left), confocal laser scanning microscopy (centre), and laser scanning microscopy (right) [109].

determined by the scattering angle of the electrons, allowing for the reconstruction of surface topography through electronic images [106]. Compared to other sensor types, such as visible or thermal-based sensors, backscattered electron (BSE) detectors demonstrate robustness, particularly in the fabrication environment characterised by high process temperatures, x-ray radiation and contamination. Furthermore, BSE detectors are unaffected by metallisation, enhancing the overall durability of the method [106]. Table 3 summarises *in-situ* measurement methods based on ELO.

Arnold *et al* [109] implemented *in-situ* ELO imaging on a custom-built PBF-EB machine equipped with a BSE sensor, offering a lateral resolution range from 50 $\mu\text{m}/\text{pixel}$ to 100 $\mu\text{m}/\text{pixel}$. The study exhibited the detection of micrometre-scale surface porosities using *in-situ* ELO imaging (see figure 7(b)). Similarly, Franke *et al* [110] focused on detecting porosities using ELO images. They utilised a BSE detector with a lateral resolution of 60 $\mu\text{m}/\text{pixel}$, which was installed in a PBF-EB machine to capture ELO images after the melting process. Areas with low intensities on the images were detected as porosities, with a minimum range of 100–200 μm .

Gardfjell *et al* [111] used an *in-situ* ELO system, utilising a BSE detector with a resolution of 1500×1500 pixels and a pixel size of $80 \times 80 \mu\text{m}$, covering a field of view of $120 \times 120 \text{mm}$. By employing image processing methods, the ELO images were analysed to detect surface impurities. The method achieved a minimum detectable feature size of around 100 μm .

3.4. Height mapping

As apparent from the imaging methods discussed in earlier sections, 2D imaging techniques offer significant information about the layer surface. Nevertheless, obtaining height information can provide extra insights into process quality in addition to the 2D data. To achieve 3D information about layer surfaces, researchers have documented various *in-situ* techniques in the literature, including fringe projection and the use of specific blade-mounted sensors.

3.4.1. Fringe projection. The fringe projection method involves the integration of a projector and one or more cameras (see figure 8(a)). In this technique, the projector emits structured light onto the layer surface of interest, typically in a one-dimensional sinusoidal fringe pattern distribution. Subsequently, the camera or cameras capture the deformed fringe pattern resulting from the interaction of light with the layer surface. Surface height values are determined by decoding the deformed fringe pattern. The computational complexity in the fringe projection method is higher than that of the other methods based on cameras, which can make this method slower [112]. Table 4 presents the *in-situ* measurement methods for PBF, employing the fringe projection technique, along with their specifications.

Land *et al* [113] used a fringe projection system consisting of an SLR camera and a digital light processing (DLP) projector for *in-situ* surface topography measurements.

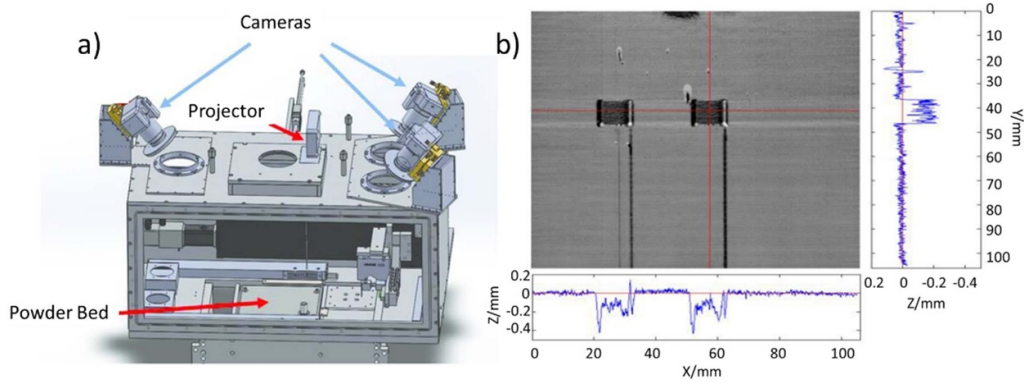


Figure 8. (a) Schematic of fringe projection integration into a PBF machine [113], (b) A portion of the imaged build area is shown as a height map in greyscale with vertical and horizontal line profiles in the right and bottom, respectively [113].

Table 4. *In-situ* measurement methods for PBF using the fringe projection technique.

References	Sensor	Resolution	Detectable features/Size range
[113]	DSLR camera and DLP projector	Noise level in vertical measurements: $\sim 18 \mu\text{m}$	Not specified
[114]	Two CCD cameras and an LCD projector	Vertical resolution: $< 10 \mu\text{m}$ Lateral resolution: $100 \mu\text{m}$	Unfused powder particles larger than $100 \mu\text{m}$
[115]	DSLR camera and DLP projector	Vertical resolution: $20 \mu\text{m}$ Lateral resolution: $60 \mu\text{m}$	Not specified
[116]	CMOS camera and DLP projector	Lateral resolution: $6.8 \mu\text{m}$	Not specified
[117]	NUB3D SIDIO XR	Point spacing: $75 \mu\text{m}$	Height variations of around $50 \mu\text{m}$
[118]	Four CMOS cameras and a DLP projector	Point spacing: $73.4 \mu\text{m}$	Not specified
[119]	Four CMOS cameras and a DLP projector	Lateral resolution: $57.62 \mu\text{m}$	Can detect defects smaller than $125 \mu\text{m}$

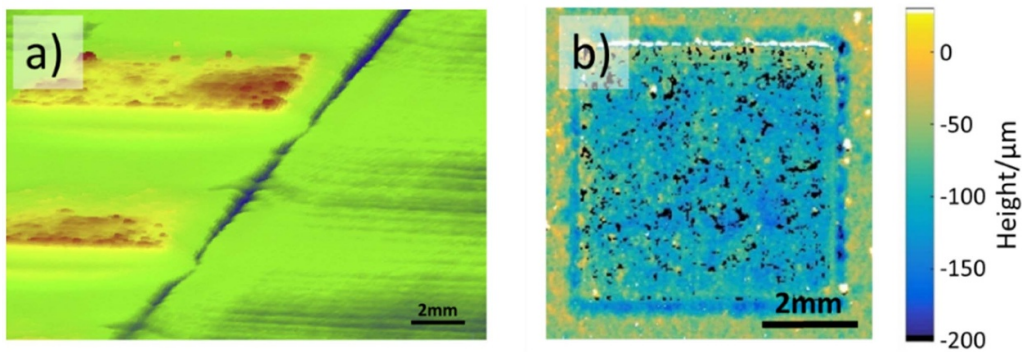


Figure 9. (a) 3D visualisation of a small section of the measurement result [114], (b) Measurement result of the *in-situ* fringe projection method [116].

This approach can detect micro-scale surface impurities (see figure 8(b)) with a noise level of approximately $18 \mu\text{m}$ in the vertical measurements.

Kalms *et al* [114] developed a fringe projection system with a vertical resolution of less than $10 \mu\text{m}$ and an approximate lateral resolution of $100 \mu\text{m}$. The fringe projection setup consisted of two 6-megapixel CCD cameras and a programmable LCD projector. Data collection was performed after both the powder deposition and melting processes. They stated that

the method can detect unfused powder particles larger than $100 \mu\text{m}$ in size (see figure 9(a)).

The fringe projection system described by Zhang *et al* [115] consists of a commercial camera with a resolution of 5184×3456 pixels positioned about 70 cm above the powder bed, along with a DLP projector with a resolution of 1280×800 pixels positioned 56 cm above the powder bed. This setup enables a lateral resolution of $60 \mu\text{m}$ and a vertical resolution of $20 \mu\text{m}$. Moreover, in a subsequent study,

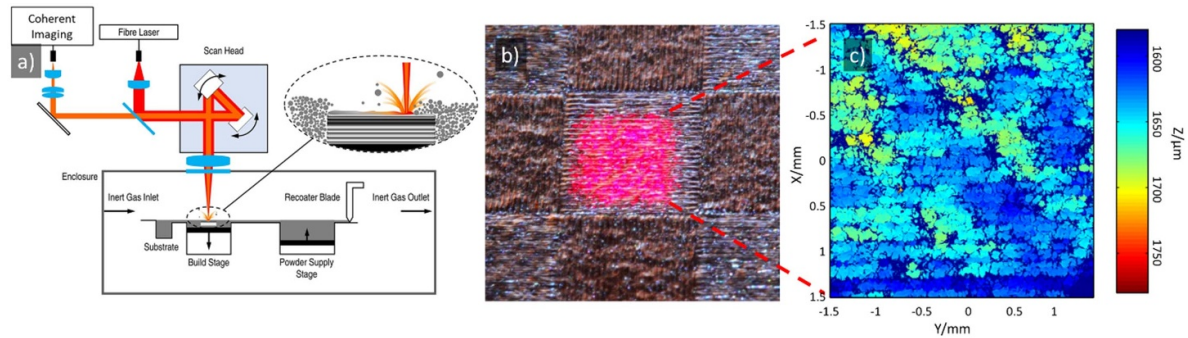


Figure 10. (a) An example of implementation of CI as *in-situ* measurement [122], (b) PBF-LB surface, (c) resulting profile scans of the structure [120].

Zhang *et al* [116] enhanced the resolution using different camera and positioning techniques. In this case, a camera with a resolution of 4096×2160 pixels was placed 20 cm above the powder bed, while a DLP projector with a resolution of 1280×800 pixels was positioned 60 cm above the powder bed. The improved arrangement achieves a lateral resolution of $6.8 \mu\text{m}/\text{pixel}$ (an example of measurement in figure 9(b)). As a result, the proposed *in-situ* surface topography measurements can be used to detect microscale surface impurities.

Southon *et al* [117] used a commercial fringe projection system (NUB3D SIDIO XR) for in-process measurement of the PBF of polymer. The fringe projection system was positioned outside the PBF machine to perform measurements, with the capability to detect height variations of around $50 \mu\text{m}$.

Dickins *et al* [118] built a multi-view fringe projection system including four cameras and a projector. A physical replica representing the build space of the Renishaw AM250 system was constructed, and the components were positioned within it. The transition from a single-camera to a multi-camera approach resulted in a reduction of the mean point spacing from $136.7 \mu\text{m}$ to $73.4 \mu\text{m}$, which indicates the potential applicability of the system in defect detection, particularly for defects larger than $100 \mu\text{m}$. Following this [118], Remani *et al* [119] improved the fringe projection method described in [118]. They reported a lateral resolution of $57.62 \mu\text{m}/\text{pixel}$ with the capability of detecting defects smaller than $125 \mu\text{m}$.

3.4.2. Coherent imaging (CI). CI, also known as low-coherence interferometry, has been applied for *in-situ* surface topography construction in PBF, as demonstrated in [120–122]. This method can be coaxially integrated into a PBF machine (see figure 10(a)), thereby eliminating the need for coordinate transformation, as required in off-axis approaches. Nevertheless, it is important to note that the integration cost can be high [31]. By employing CI, surface height values are obtained through raster scanning of the layer surface with light. The interference between the backscattered imaging and a reference light beam, caused by the optical path difference, can be encoded to calculate layer surface heights. Detailed

information about the working principle of CI can be found elsewhere [123].

Neef *et al* [120] used a CI method for *in-situ* measurement with a broadband light source utilising the same optical path as the processing beam of PBF. The CI sensor in this study can scan a $3 \times 3 \text{ mm}$ area with a sampling distance of $4 \mu\text{m}$ (see figures 10(b) and (c)). The resulting height map detected single powder particles as small as $20\text{--}40 \mu\text{m}$. Similarly, DePond *et al* [121] implemented CI to a larger area, specifically a $4.4 \times 4.4 \text{ cm}$ area. The scanning was performed after switching off the processing laser, which reduces the overall fabrication speed. The system in this study demonstrated an axial resolution of $25 \mu\text{m}$ and a lateral resolution of $100 \mu\text{m}$, with a scan speed of 1 m s^{-1} . The study highlights that the method can detect spatters within the size range from $200 \mu\text{m}$ to $700 \mu\text{m}$.

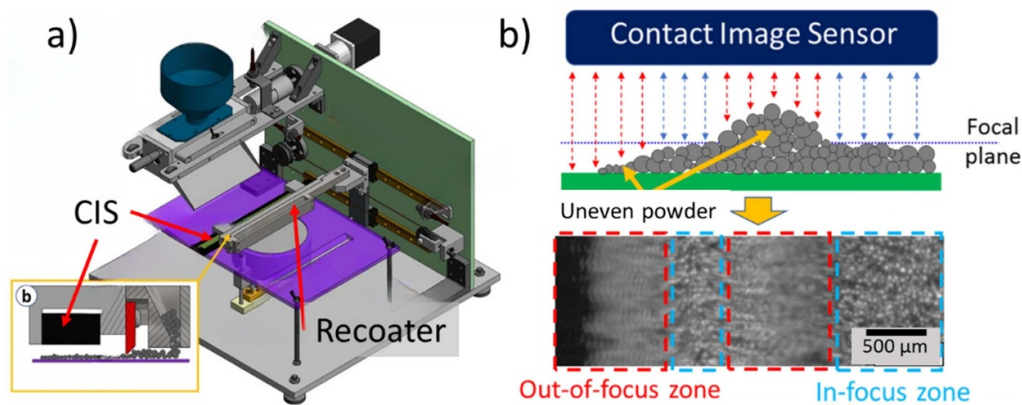
Fleming *et al* [122] developed a manual closed-loop control system utilising a CI method. This system could detect microscale protrusions and recesses using a CI system with vertical and lateral resolution of $7 \mu\text{m}$ and $30 \mu\text{m}$, respectively. Subsequently, the system compensated for detected impurities manually by applying additional processes.

3.4.3. Blade-mounted sensing. Another method for measuring surface height values involves mounting a sensor on the PBF machine's recoater blade. These sensors utilise the motion of the blade as the scanning direction of the surface. Table 5 shows the *in-situ* measurement methods for PBF, employing CI and blade-mounted sensors, with their respective specifications. Barrett *et al* [124] used this approach by mounting a laser line scan profilometer, employing the triangulation method, on the recoater blade to obtain powder bed height measurements after melting. The scanner's spanning width was 15 mm , and the lateral profile data interval was $20 \mu\text{m}$. This study shows that blade-mounted sensing has the potential to detect LOF and spatters.

Phuc *et al* [125] introduced a practical blade-mounted sensing system which employed a contact image sensor. The sensor was detached from a flatbed document scanner and mounted onto a recoater blade (see figure 11(a)). The study

Table 5. *In-situ* measurement methods for PBF using coherent and blade-mounted sensors.

References	Sensor	Resolution	Detectable features/ Size range
[120]	Coherent imaging	Sampling distance: 4 μm	20–40 μm
[121]	Coherent imaging	Vertical resolution: 25 μm lateral resolution: 100 μm	200–700 μm
[122]	Coherent imaging	Vertical resolution: 7 μm lateral resolution: 30 μm	Not specified
[124]	Blade-mounted laser scan profilometry	Lateral profile data interval: 20 μm	An ellipse with a size of 1.00 \times 0.25 mm
[125]	Blade-mounted contact image sensor	Spatial Resolution: \sim 5 μm	\sim 14 μm

**Figure 11.** (a) Computer-aided design of the experimental setup used for the powder bed scanner, (b) schematic cross-section view of a layer and its corresponding top-view scan [125].**Table 6.** *In-situ* measurement methods for PBF using acoustic sensors.

References	Sensor	Detectable features/Size range	Detection method/ algorithm
[78]	Microphone	Balling and overheating on single weld tracks	Deep belief network model
[126]	Microphone	Balling on single weld tracks	Signal processing algorithms on LabView
[127]	Spatially resolved acoustic spectroscopy	Pores and cracks	Image processing

explored the impact of varying scanning speeds on spatial resolution. The highest spatial resolution achieved was approximately 5 μm , with the ability to resolve features of approximately 14 μm in size. This study's height data was derived from the degree of blurriness observed in the acquired images (see figure 11(b)).

3.5. Acoustic sensing

Acoustic sensors are applicable for *in-situ* measurements in PBF. However, the data provided by these sensors might be challenging to interpret due to the absence of visual information, in contrast to sensors such as visible or thermal imaging sensors. Unlike imaging sensors, acoustic sensors do not require direct observation of the layer surface, so

they offer more flexible positioning. Yet, factors such as acoustic reflection and resonance must be considered when designing these sensors' positions [126]. Table 6 presents the *in-situ* measurement methods for PBF, employing acoustic sensors, along with the features of interest and detection algorithms.

Ye *et al* [78] installed a microphone into a PBF-LB machine to collect *in-situ* acoustic signals. Weld tracks with different morphologies, including tracks with balling and overheating defects, as well as a defect-free weld track, were produced. The acoustic signals of five different weld tracks were classified using a deep belief network model, achieving classification rates of approximately 70% for the original data and 95% for the data after applying the fast Fourier transform and denoising algorithms.

Table 7. *In-situ* measurement methods for PBF using a combination of sensing methods.

References	Sensor	Resolution	Detectable features/ Size range	Detection method/ algorithm
[128]	Combination of visible, infrared, and polarisation imaging	Pixel size on visible range imaging: 1.1 μm Pixel size on infrared range imaging: 30 μm Pixel size on polarisation imaging: 3.45 μm	$\sim 40 \mu\text{m}$	Image processing
[129]	Combination of visible range imaging, acoustic sensing, multi-spectral emission sensing, and laser scan vector data	Spatial resolution on visible range imaging: 10 $\mu\text{m}/\text{pixel}$	$\sim 30 \mu\text{m}$	Neural network
[130]	Combination of visible range imaging, multi-spectral emission sensing, and laser scan vector data	Spatial resolution of visible range imaging: 62.5 \times 62.5 μm	$> \sim 200 \mu\text{m}$	Convolutional neural network

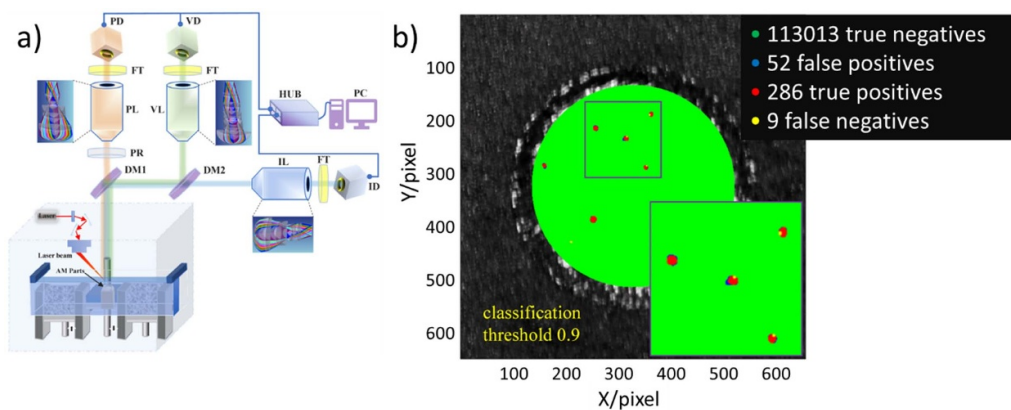


Figure 12. (a) Schematic diagram of the multi-sensor system: PL: polarization channel imaging system; IL: infrared channel imaging system; VL: visible channel imaging system; DM1: beamsplitter 1; DM2: beamsplitter 2; FT: filters; ID: infrared channel image sensor; PD: polarization channel image sensor; VD: visible channel image sensor; PR: polarizer; PC: computer [128], (b) neural network prediction of defects on a layer (10 μm per pixel) [129].

Similarly, Koupryanoff *et al* [126] focused on analysing the acoustic signals of weld tracks with various qualities. The anomalies, such as balling and irregular weld tracks, were detected from acoustic signals using the signal processing algorithms in LabView.

In a study conducted by Pieris *et al* [127], the capability of spatially resolved acoustic spectroscopy (SRAS), a laser ultrasonic technique, in the online measurement of PBF-LB was investigated. They utilised PBF-LB parts with polished surfaces and manufactured them using various laser power and hatching strategies. The findings indicated that SRAS is capable of identifying not only microscale surface impurities (such as cracking and unfused powders) but also sub-surface anomalies (such as pores).

3.6. Combination of methods

In addition to employing individual sensing methods, researchers have proposed integrating multiple sensing techniques to enhance defect detection accuracy. Combining different sensing methods, each with unique strengths, can overcome the limitations inherent in each technique. Table 7 outlines the *in-situ* measurement techniques for PBF discussed in this section, along with their specifications. Peng and Kong [128] developed a coaxial multi-sensor defect detection system, integrating visible, IR and polarisation imaging systems (see figure 12(a)). It has been demonstrated that multi-sensor systems exhibit superior results in extracting micro-scale defects, such as cracking, scratches and porosity, compared to individual sensor systems.

Petrich *et al* [129] integrated visible range, acoustic and multi-spectral emission sensors to collect *in-situ* layer images, acoustic and laser emission data. Following data preprocessing, a ML algorithm was trained for defect detection using the *in-situ* data, scanning vector data and *ex-situ* XCT data as ‘ground truth’. It has achieved more than 98% accuracy for the binary classification of the surface status. A prediction result of the algorithm of a layer with a classification threshold of 0.9 can be seen in figure 12(b). This study also presented the contributions of each sensing method to the performance of the defect detection algorithm and concluded that visible imaging demonstrates the highest contribution.

Snow *et al* [130] used a combination of *in-situ* data, including visible range images, multi-spectral emissions, and laser scan vector data, and established correlations between these data and fatigue performance. The convolutional neural network has been used as a classifier to detect defects. The minimum detectable defect size was limited to 200 μm by the camera resolution. The best classifier they trained exhibited a 100% accurate prediction for defects of 380 μm and above.

Lastly, Remani *et al* [29] combined three *in-situ* measurement methods: fringe projection and thermal imaging for measuring layers and visible imaging for measuring melt pools. Their preliminary findings indicated that the system can be used to detect surface impurities such as protrusions and recesses.

4. Discussion and conclusion

This paper summarises the microscale surface impurities generated during the PBF process, along with their formation mechanisms and influence on the quality of the fabricated parts. *In-situ* measurement methodologies, which provide detection of these microscale surface impurities, are reviewed, along with their capabilities and limitations, and summarised in table 8. Visible and thermal sensing methods are the most used *in-situ* measurement methods as they can produce a large amount of data when using high-resolution and high-speed sensors. It is essential to mention that the arrangement of cameras and lighting significantly influences detection accuracy in imaging. Variations in these configurations across different machines can affect brightness and contrast, resulting in varying detection quality from one machine to another. BSE sensors show robustness in harsh environments; however, it should be noted that these sensors can occasionally overestimate the dimensions of porosities, and beam current and voltage can influence the BSE-acquired data, leading to unstable results. Acoustic sensing, which benefits from positioning flexibility, offers a cost-effective method for detecting impurities. Nevertheless, current research involving acoustic sensors for detecting microscale impurities is limited to single weld tracks, potentially needing to capture real-world construction conditions.

Unlike 2D imaging techniques, 3D height mapping of the surface provides additional information by revealing variations in surface elevation, which is particularly important for detecting impurities as they often lead to changes in surface height. Various methods for measuring surface topography in PBF, including CI, fringe projection and blade-mounted systems, are discussed in detail. Among these methods, CI, as a coaxial approach, can be costlier to integrate. The fringe projection system might entail longer computation times than other methods, and installing projectors and cameras into a PBF machine can also be challenging. Blade-mounted systems, however, have resolution tied to the recoater’s speed.

In-situ measurement and monitoring methods for detecting microscale impurities have been presented, each with its own advantages and limitations. However, there are significant gaps in general in the applicability of these methods in real-world industrial fabrication settings. While most methods collect data in real-time, the actual detection often occurs afterwards due to the high computational costs involved. Moreover, many studies do not specify the time required for detection, making it impractical to implement these methods as real-time feedback control systems.

Additionally, variations in materials, process parameters, sensor positioning, and machine types can impact the sensor’s efficiency and the detection accuracy of the algorithms. The installation of sensors may also be challenging or impossible on certain machines. For methods employing ML algorithms to detect impurities, generating datasets for training supervised ML algorithms presents an additional challenge. This process often relies on manual input from human operators, making it time-consuming and subjective. Even with unsupervised learning, a significant amount of data is still required to effectively train ML algorithms effectively.

In section 2, certain microscale surface impurities, along with their influences on part quality, have been presented. It has been reported some impurities are even smaller than 10 μm . However, the accuracy of most detection methods diminishes as the size of the impurity decreases, especially when it falls below 100 μm mostly due to their resolution limits. In order to provide a robust evaluation system, detection accuracy needs to be stable. On the other hand, real-time detection is also desired to meet the industry criteria. However, instead of detecting only some specific defects, the detection method needs to target all microscale impurities (even smaller than 100 μm in size) to be a general quality evaluation system. In order to meet the demands from industry, further research is necessary to develop a measurement system capable of providing surface topography information, detecting small features with consistently high accuracy, and doing so efficiently and cost-effectively.

Our future work will focus on employing a light scattering model combined with unsupervised ML algorithms trained on simulated data from synthetically generated surfaces to detect microscale impurities even as small as 10 μm . This approach aims to overcome several challenges, including the need for

Table 8. Overview of *in-situ* measurement methods' principal benefits and drawbacks.

Sensing Method	Benefits	Drawbacks
Visible imaging	Straightforward implementation	High-resolution and high-speed sensors generate large datasets Detection efficiency varies due to the arrangement of cameras and lighting, resulting in varying detection qualities among machines
Thermal imaging	Identification of thermal signatures	High-resolution and high-speed sensors generate large datasets
Electronic imaging	BSE sensors demonstrate robustness in harsh environments	BSE-acquired data can be influenced by beam current and voltage
Fringe projection	Generation of height maps	Installation of projectors and cameras into a PBF machine can be challenging Longer computation times
Coherent imaging	Generation of height maps	Integration of this coaxial method may incur higher costs
Blade mounted sensing	Generation of height maps	Resolution is dependent on the movement and speed of the recoater
Acoustic sensing	Offers positioning flexibility Cost-effective method	Limited applicability to single weld track experiments
Combined sensing	Overcomes limitations of individual sensing methods	Registration of different types of data is required Large amount of data from different sensors

experimental datasets to train ML algorithms while offering a fast, cost-effective, and computationally efficient solution.

Data availability statement

No new data were created or analysed in this study.

Acknowledgments

Ahmet Koca would like to acknowledge the support from The Republic of Türkiye Ministry of National Education [35373136]. The authors would like to thank the support from the European Commission [AI-SURF, 101054454] and The Royal Society [IES\R2\232123, ICA\R1\231038].

Conflict of interest

The authors declare that they have no known competing financial interests or personal relationships that could have appeared to influence the work reported in this paper.

CRedit authorship contribution statement

Ahmet Koca: Writing—original draft, Conceptualization, Investigation. **Helia Hooshmand:** Supervision, Writing—review & editing, Conceptualization. **Richard Leach:** Supervision, Writing—review & editing, Conceptualization, Funding acquisition. **Mingyu Liu:** Supervision, Writing—review & editing, Conceptualization, Funding acquisition.

Appendix

The specification of *in-situ* methods

References	Sensor	Resolution	Detectable features/Size range	Detection method/algorithm	Detection Accuracy
[83]	Monochrome CCD Camera	Spatial resolution: ~30 $\mu\text{m}/\text{pixel}$	>90 μm	Image processing	Not specified
[84]	Single-Lens Reflex Camera	Spatial resolution: 10–13 $\mu\text{m}/\text{pixel}$	~500 μm	Image processing	Not specified
[85]	DSLR Camera	Spatial resolution: ~62.5 $\mu\text{m}/\text{pixel}$	$\geq 40 \mu\text{m}$	CNN	Depends on the size: for ~40 μm less than 50%, for ~200 μm around 90%, for larger than 475 μm 100% Around 87% detection accuracy
[86]	DSLR Camera	Pixel size range: 45 \times 47 μm –67 \times 88 μm	50–750 μm	Image processing	Not specified
[87]	Monochrome CCD Camera	Not specified	$\geq 10 \mu\text{m}$	Particle analysis	Not specified
[88]	Line Camera	Spatial resolution: 5.97 $\mu\text{m}/\text{pixel}$	$\geq 12.4 \mu\text{m}$	Feature-based analysis	Not specified
[104]	NIR range imaging	Not specified	>~200 μm	Image processing	79% of detection
[102]	IR range imaging	Not specified	Spatters from 0.1 $\times 10^6 \mu\text{m}^2$ to 2.0 $\times 10^6 \mu\text{m}^2$	Image analysis software (MIPAR)	Not specified
[99]	NIR range imaging	Not specified	>100 μm	Image processing	Not specified
[103]	IR range imaging	Not specified	600–900 μm	Image processing	100%
[96]	IR range imaging	Not specified	>~300 μm	Manual analysis (by looking at the graphs)	Not specified
[105]	NIR range imaging	Not specified	150 μm (can detect smaller features with low accuracy)	A specific algorithm was developed to correlate the OT and x-ray tomography data	90/95% probability of detection
[101]	IR range imaging	Not specified	50–500 μm	Image processing	Depends on the size: for <50 μm , less than 50%; for >500 μm , 100%
[100]	IR range imaging	Not specified	750 μm	Image processing	Not specified
[109]	BSE sensor	Not specified	~300 μm	Based on the correlation between ELO images, optical images, and surface topography data	Not specified
[110]	BSE sensor	Not specified	100–200 μm	Based on the correlation between ELO images and optical images	Not specified
[111]	BSE sensor	Not specified	>~100 μm	Image processing (contour identification, edge detection)	Not specified
[113]	1 DSLR camera, 1 DLP projector	Noise level of approximately 18 μm in vertical measurements	Not specified	Not specified	Not specified
[114]	2 CCD cameras, 1 LCD projector	Vertical resolution of less than 10 μm and lateral resolution of 100 μm	Unfused powder particles larger than 100 μm in size	Not specified	Not specified

(Continued.)

(Continued.)

References	Sensor	Resolution	Detectable features/Size range	Detection method/algorithm	Detection Accuracy
[115]	1 DSLR camera, 1 DLP projector	Vertical resolution of 20 μm and lateral resolution of 60 μm	Not specified	Not specified	Not specified
[116]	1 CMOS camera, 1 DLP projector	Lateral resolution of 6.8 $\mu\text{m}/\text{pixel}$	Not specified	Not specified	Not specified
[117]	NUB3D SIDIO XR	Point spacing of 75 μm	Height variations of around 50 μm	Not specified	Not specified
[118]	4 CMOS cameras, 1 DLP projector	Point spacing of 73.4 μm	Not specified	Not specified	Not specified
[119]	4 CMOS cameras, 1 DLP projector	Lateral resolution of 57.62 $\mu\text{m}/\text{pixel}$	Can detect defects smaller than 125 μm	Not specified	Not specified
[120]	Coherent Imaging	Sampling Distance: 4 μm	20–40 μm	Not specified	Not specified
[121]	Coherent Imaging	Vertical Resolution: 25 μm Lateral Resolution: 100 μm	200–700 μm	Not specified	Not specified
[122]	Coherent Imaging	Vertical Resolution: 7 μm Lateral Resolution: 30 μm	Not specified	Not specified	Not specified
[124]	Blade-Mounted Laser Scan Profilometry	Lateral Profile Data Interval: 20 μm	An ellipse with the size of 1.0 \times 0.25 mm can be detected	Not specified	Not specified
[125]	Blade-Mounted Contact Image Sensor	Spatial Resolution: \sim 5 μm	\sim 14 μm	Not specified	Not specified
[78]	Microphone		Balling and overheating on single weld tracks	Deep belief network model	Not specified
[126]	Microphone		Balling on single weld tracks	Signal processing algorithms on LabView	Not specified
[127]	Spatially resolved acoustic spectroscopy		Pores and cracks	Image processing	Not specified
[128]	Combination of visible, infrared, and polarization imaging	Pixel size on visible range imaging: 1.1 μm , pixel size on infrared range imaging: 30 μm , pixel size on polarization imaging: 3.45 μm	\sim 40 μm	Image processing	Not specified
[129]	Combination of visible range imaging, acoustic sensing, multi-spectral emission sensing, and laser scan vector data	Spatial resolution on visible range imaging: 10 $\mu\text{m}/\text{pixel}$	\sim 30 μm	NN	Not specified
[130]	Combination of visible range imaging, multi-spectral emission sensing, and laser scan vector data	Spatial resolution of visible range imaging: 62.5 \times 62.5 μm	$>$ \sim 200 μm	CNN	Not specified

ORCID iDs

Ahmet Koca  <https://orcid.org/0000-0003-2836-8619>

Mingyu Liu  <https://orcid.org/0000-0001-8188-9953>

References

- [1] Gibson I, Rosen D and Stucker B 2015 *Additive Manufacturing Technologies: 3D Printing, Rapid Prototyping, and Direct Digital Manufacturing* 2nd edn (Springer)
- [2] Bourell D L 2016 Perspectives on additive manufacturing *Annu. Rev. Mater. Res.* **46** 1–18
- [3] Wohlers T W 2024 *Wohlers Report 2024* Wohlers Associates
- [4] Toyserkani E, Sarker D, Obehi Ibhadode O, Liravi F, Russo P and Taherkhani K 2021 *Metal Additive Manufacturing* (Wiley)
- [5] Everton S K, Hirsch M, Stavroulakis P I, Leach R K and Clare A T 2016 Review of in-situ process monitoring and in-situ metrology for metal additive manufacturing *Mater. Des.* **95** 431–45
- [6] Snow Z, Nassar A R and Reutzel E W 2020 Invited Review Article: review of the formation and impact of flaws in powder bed fusion additive manufacturing *Addit. Manuf.* **36** 101457
- [7] Berez J and Saldaña C 2024 On the nature and causes of spatter redistribution in laser powder bed fusion *J. Manuf. Process.* **127** 531–44
- [8] Leach R and Carmignato S 2020 *Precision Metal Additive Manufacturing* (CRC Press) (available at: <http://ebookcentral.proquest.com/lib/nottingham/detail.action?docID=6272924>)
- [9] Gu D and Shen Y 2009 Balling phenomena in direct laser sintering of stainless steel powder: metallurgical mechanisms and control methods *Mater. Des.* **30** 2903–10
- [10] Wang D, Wu S, Fu F, Mai S, Yang Y, Liu Y and Song C 2017 Mechanisms and characteristics of spatter generation in SLM processing and its effect on the properties *Mater. Des.* **117** 121–30
- [11] Moon S, Ma R, Attardo R, Tomonto C, Nordin M, Wheelock P, Glavicic M, Layman M, Billo R and Luo T 2021 Impact of surface and pore characteristics on fatigue life of laser powder bed fusion Ti–6Al–4V alloy described by neural network models *Sci. Rep.* **11** 20424
- [12] Niendorf T and Brenne F 2013 Steel showing twinning-induced plasticity processed by selective laser melting—An additively manufactured high performance material *Mater. Charact.* **85** 57–63
- [13] Zhou J, Han X, Li H, Liu S, Shen S, Zhou X and Zhang D 2021 In-situ laser polishing additive manufactured alsi10mg: effect of laser polishing strategy on surface morphology, roughness and microhardness *Materials* **14** 1–19
- [14] Zhang H, Xu M, Liu Z, Li C, Kumar P, Liu Z and Zhang Y 2021 Microstructure, surface quality, residual stress, fatigue behavior and damage mechanisms of selective laser melted 304L stainless steel considering building direction *Addit. Manuf.* **46** 102147
- [15] Molaei R and Fatemi A 2019 Crack paths in additive manufactured metallic materials subjected to multiaxial cyclic loads including surface roughness, HIP, and notch effects *Int. J. Fatigue* **124** 558–70
- [16] Li Z 2022 A review of spatter in laser powder bed fusion additive manufacturing: in situ detection, generation, effects, and countermeasures *Micromachines* **13** 1366
- [17] Fotovvati B, Namdari N and Dehghanhadikolaei A Fatigue performance of selective laser melted Ti6Al4V components: state of the art *Mater. Res. Express* **6** 2019
- [18] Zhang H, Xu M, Kumar P, Li C, Liu Z and Zhang Y 2021 Fatigue life prediction model and entropy generation of 304L stainless steel fabricated by selective laser melting *J. Mater. Process. Technol.* **297** 117279
- [19] Sanviemvongsak T, Monceau D, Madelain M, Desgranges C, Smialek J and Macquaire B 2021 Cyclic oxidation of alloy 718 produced by additive manufacturing compared to a wrought-718 alloy *Corros. Sci.* **192** 109804
- [20] Romano S, Nezhadfar P D, Shamsaei N, Seifi M and Beretta S 2020 High cycle fatigue behavior and life prediction for additively manufactured 17-4 PH stainless steel: effect of sub-surface porosity and surface roughness *Theor. Appl. Fract. Mech.* **106** 102477
- [21] Zhu Z, Lou S and Majewski C 2020 Characterisation and correlation of areal surface texture with processing parameters and porosity of high speed sintered parts *Addit. Manuf.* **36** 101402
- [22] Fritsch T, Farahbod-Sternahl L, Serrano-Muñoz I, Léonard F, Haberland C and Bruno G 2022 3D computed tomography quantifies the dependence of bulk porosity, surface roughness, and re-entrant features on build angle in additively manufactured IN625 lattice struts *Adv. Eng. Mater.* **24** 2100689
- [23] Thompson A, Maskery I and Leach R K 2016 X-ray computed tomography for additive manufacturing: a review *Meas. Sci. Technol.* **27** 072001
- [24] Mirabal A, Loza-Hernandez I, Clark C, Hooks D E, McBride M and Stull J A 2023 Roughness measurements across topographically varied additively manufactured metal surfaces *Addit. Manuf.* **69** 103540
- [25] Flys O, Berglund J and Rosen B G 2020 Using confocal fusion for measurement of metal AM surface texture *Surf. Topogr.* **8** 024003
- [26] Newton L, Thanki A, Bermudez C, Artigas R, Thompson A, Haitjema H and Leach R 2023 Optimisation of imaging confocal microscopy for topography measurements of metal additive surfaces *Metrology* **3** 186–221
- [27] Aguado-Montero S, Navarro C, Vázquez J and Domínguez J 2021 Experimental and numerical analysis of fatigue cracks emanating from internal defects in Ti6Al4V SLM *Proc. Struct. Integr.* **34** 121–8
- [28] Narasimharaju S R, Liu W, Zeng W, See T L, Scott P, Jiang X J and Lou S 2021 Surface texture characterization of metal selective laser melted part with varying surface inclinations *J. Tribol.* **143** 051106
- [29] Remani A, Williams R, Rossi A and Peña F 2022 Multi-sensor measurement for in-situ defect identification in metal laser powder bed fusion (ASPE/Euspen) (available at: www.researchgate.net/publication/362133370)
- [30] Grasso M and Colosimo B M 2017 Process defects and in situ monitoring methods in metal powder bed fusion: a review *Meas. Sci. Technol.* **28** 044005
- [31] Peng X, Kong L, An H and Dong G 2022 A review of in situ defect detection and monitoring technologies in selective laser melting *3D Print Addit. Manuf.* **10** 438–66
- [32] Melvin III L S, Das S and Beaman J J 1994 Video microscopy of selective laser sintering *Int. Solid Freeform Fabrication Symp.*
- [33] Benda J A 1994 Temperature-controlled selective laser sintering *Int. Solid Freeform Fabrication Symp.*
- [34] Tapia G and Elwany A 2014 A review on process monitoring and control in metal-based additive manufacturing *J. Manuf. Sci. Eng. Trans. ASME* **136** 060801
- [35] Berumen S, Bechmann F, Lindner S, Kruth J P and Craeghs T 2010 Quality control of laser- and powder bed-based additive manufacturing (AM) technologies *Phys. Proc.* **5** 617–22

- [36] Grasso M, Remani A, Dickins A, Colosimo B M and Leach R K 2021 In-situ measurement and monitoring methods for metal powder bed fusion: an updated review *Meas. Sci. Technol.* **32** 112001
- [37] Zhang X, Cheng B and Tuffile C 2020 Simulation study of the spatter removal process and optimization design of gas flow system in laser powder bed fusion *Addit. Manuf.* **32** 101049
- [38] Liu Y, Yang Y, Mai S, Wang D and Song C 2015 Investigation into spatter behavior during selective laser melting of AISI 316L stainless steel powder *Mater. Des.* **87** 797–806
- [39] Lutter-Günther M, Bröker M, Mayer T, Lizak S, Seidel C and Reinhart G 2018 Spatter formation during laser beam melting of AlSi10Mg and effects on powder quality *Proc. CIRP* **74** 33–38
- [40] Qiu C, Panwisawas C, Ward M, Basoalto H C, Brooks J W and Attallah M M 2015 On the role of melt flow into the surface structure and porosity development during selective laser melting *Acta Mater.* **96** 72–79
- [41] Ratsimba A, Zerrouki A, Tessier-Doyen N, Nait-Ali B, André D, Dupont P, Neveu A, Tripathi N, Francqui F and Delaizir G 2021 Densification behaviour and three-dimensional printing of Y₂O₃ ceramic powder by selective laser sintering *Ceram. Int.* **47** 7465–74
- [42] Shuai L, Qinghong J, Sai G, Bi Z and Cong Z 2022 Effect of spattering on formation mechanisms of metal matrix composites in laser powder bed fusion *J. Mater. Process. Technol.* **304** 117533
- [43] Attar H, Calin M, Zhang L C, Scudino S and Eckert J 2014 Manufacture by selective laser melting and mechanical behavior of commercially pure titanium *Mater. Sci. Eng.* **593** 170–7
- [44] Guo C, Xu Z, Zhou Y, Shi S, Li G, Lu H, Zhu Q and Ward R M 2021 Single-track investigation of IN738LC superalloy fabricated by laser powder bed fusion: track morphology, bead characteristics and part quality *J. Mater. Process. Technol.* **290** 117000
- [45] Ali U, Esmailizadeh R, Ahmed F, Sarker D, Muhammad W, Keshavarzkermani A, Mahmoodkhani Y, Marzbanrad E and Toyserkani E 2019 Identification and characterization of spatter particles and their effect on surface roughness, density and mechanical response of 17-4PH stainless steel laser powder-bed fusion parts *Mater. Sci. Eng.* **756** 98–107
- [46] Rafi H K, Gong H, Rafi K, Starr T and Stucker B 2013 The effects of processing parameters on defect regularity in Ti-6Al-4V parts fabricated by selective laser melting and electron beam melting *24th Annual Int. Solid Freeform Fabrication Symp.* (available at: www.researchgate.net/publication/272167481)
- [47] Ladewig A, Schlick G, Fisser M, Schulze V and Glatzel U 2016 Influence of the shielding gas flow on the removal of process by-products in the selective laser melting process *Addit. Manuf.* **10** 1–9
- [48] Li L, Li J Q and Fan T H 2021 Phase-field modeling of wetting and balling dynamics in powder bed fusion process *Phys. Fluids* **33** 042116
- [49] Liu S and Guo H 2020 Balling behavior of selective laser melting (SLM) magnesium alloy *Materials* **13** 3632
- [50] Li R, Liu J, Shi Y, Wang L and Jiang W 2012 Balling behavior of stainless steel and nickel powder during selective laser melting process *Int. J. Adv. Manuf. Technol.* **59** 1025–35
- [51] Li R, Shi Y, Wang Z, Wang L, Liu J and Jiang W 2010 Densification behavior of gas and water atomized 316L stainless steel powder during selective laser melting *Appl. Surf. Sci.* **256** 4350–6
- [52] Pal S, Lojen G, Hudak R, Rajtukova V, Brajljih T, Kokol V and Drstvenšek I 2020 As-fabricated surface morphologies of Ti-6Al-4V samples fabricated by different laser processing parameters in selective laser melting *Addit. Manuf.* **33** 101147
- [53] Tian Y, Tomus D, Rometsch P and Wu X 2017 Influences of processing parameters on surface roughness of Hastelloy X produced by selective laser melting *Addit. Manuf.* **13** 103–12
- [54] Bi J, Lei Z, Chen Y, Chen X, Qin X and Tian Z 2019 Effect of process parameters on formability and surface quality of selective laser melted Al-Zn-Sc-Zr alloy from single track to block specimen *Opt. Laser Technol.* **118** 132–9
- [55] Skalon M, Meier B, Gruberbauer A, Amancio-Filho S T and Sommitsch C 2020 Stability of a melt pool during 3D-printing of an unsupported steel component and its influence on roughness *Materials* **13** 808
- [56] Li G, Li X, Guo C, Zhou Y, Tan Q, Qu W, Li X, Hu X, Zhang M X and Zhu Q 2022 Investigation into the effect of energy density on densification, surface roughness and loss of alloying elements of 7075 aluminium alloy processed by laser powder bed fusion *Opt. Laser Technol.* **147** 107621
- [57] Mumtaz K and Hopkinson N 2009 Top surface and side roughness of Inconel 625 parts processed using selective laser melting *Rapid Prototyp. J.* **15** 96–103
- [58] Yuan W, Chen H, Cheng T and Wei Q 2020 Effects of laser scanning speeds on different states of the molten pool during selective laser melting: simulation and experiment *Mater. Des.* **189** 108542
- [59] Wu H, Li J, Wei Z and Wei P 2020 Effect of processing parameters on forming defects during selective laser melting of AlSi10Mg powder *Rapid Prototyp. J.* **26** 871–9
- [60] Gasper A N D, Szost B, Wang X, Johns D, Sharma S, Clare A T and Ashcroft I A 2018 Spatter and oxide formation in laser powder bed fusion of Inconel 718 *Addit. Manuf.* **24** 446–56
- [61] Nassar A R, Gundermann M A, Reutzel E W, Guerrier P, Krane M H and Weldon M J 2019 Formation processes for large ejecta and interactions with melt pool formation in powder bed fusion additive manufacturing *Sci. Rep.* **9** 5038
- [62] Gasper A N D, Hickman D, Ashcroft I, Sharma S, Wang X, Szost B, Johns D and Clare A T 2019 Oxide and spatter powder formation during laser powder bed fusion of Hastelloy X *Powder Technol.* **354** 333–7
- [63] Yin J, Wang D, Yang L, Wei H, Dong P, Ke L, Wang G, Zhu H and Zeng X 2020 Correlation between forming quality and spatter dynamics in laser powder bed fusion *Addit. Manuf.* **31** 100958
- [64] Thanki A, Goossens L, Ompusunggu A P, Bayat M, Bey-Temsamani A, Van Hooreweder B, Kruth J P and Witvrouw A 2022 Melt pool feature analysis using a high-speed coaxial monitoring system for laser powder bed fusion of Ti-6Al-4 V grade 23 *Int. J. Adv. Manuf. Technol.* **120** 6497–514
- [65] Esmailizadeh R, Ali U, Keshavarzkermani A, Mahmoodkhani Y, Marzbanrad E and Toyserkani E 2019 On the effect of spatter particles distribution on the quality of Hastelloy X parts made by laser powder-bed fusion additive manufacturing *J. Manuf. Process.* **37** 11–20
- [66] Leung C L A, Marussi S, Towrie M, Atwood R C, Withers P J and Lee P D 2019 The effect of powder oxidation on defect formation in laser additive manufacturing *Acta Mater.* **166** 294–305
- [67] Qiu C, Adkins N J E and Attallah M M 2013 Microstructure and tensile properties of selectively laser-melted and of HIPed laser-melted Ti-6Al-4V *Mater. Sci. Eng.* **578** 230–9
- [68] Leung C L A, Marussi S, Atwood R C, Towrie M, Withers P J and Lee P D 2018 In situ x-ray imaging of defect and molten pool dynamics in laser additive manufacturing *Nat. Commun.* **9** 1355

- [69] Zhou H, Su H, Guo Y, Liu Y, Zhao D, Yang P, Shen Z, Xia L and Guo M 2023 Formation and evolution of surface morphology in overhang structure of IN718 superalloy fabricated by laser powder bed fusion *Acta Metall. Sin.* **36** 1433–53
- [70] Sun X, Zhou W, Kikuchi K, Nomura N, Kawasaki A, Doi H, Tsutsumi Y and Hanawa T 2017 Fabrication and characterization of a low magnetic Zr-1Mo alloy by powder bed fusion using a fiber laser *Metals* **7** 501
- [71] Rothfelder R, Baumgärtner B, Hausotte T and Schmidt M 2022 Surface layer porosity and surface quality in dependency of contour scanning strategy of Ti6Al4V parts *Proc. CIRP* **111** 41–46
- [72] Xia M, Gu D, Yu G, Dai D, Chen H and Shi Q 2017 Porosity evolution and its thermodynamic mechanism of randomly packed powder-bed during selective laser melting of Inconel 718 alloy *Int. J. Mach. Tools Manuf.* **116** 96–106
- [73] Sun X, Zeng T, Zhou Y, Zhang K, Xu G, Wang X and Cheng S 2020 3D printing of porous SiC ceramics added with SiO₂ hollow microspheres *Ceram. Int.* **46** 22797–804
- [74] Khimich M A *et al* 2021 Advances in laser additive manufacturing of ti-nb alloys: from nanostructured powders to bulk objects *Nanomaterials* **11** 1159
- [75] Mani M, Lane B, Donmez A, Feng S, Moylan S and Feserman R 2015 Measurement science needs for real-time control of additive manufacturing powder bed fusion processes *NIST Interagency/Internal Report* (<https://doi.org/10.6028/NIST.IR.8036>)
- [76] Zhirmov I, Panahi N, Åsberg M and Krakhmalev P 2022 Process quality assessment with imaging and acoustic monitoring during laser powder bed fusion *Proc. CIRP* **111** 363–7
- [77] Wasmer K, Le-Quang T, Meylan B and Shevchik S A 2019 In situ quality monitoring in AM using acoustic emission: a reinforcement learning approach *J. Mater. Eng. Perform.* **28** 666–72
- [78] Ye D, Hong G S, Zhang Y, Zhu K and Fuh J Y H 2018 Defect detection in selective laser melting technology by acoustic signals with deep belief networks *Int. J. Adv. Manuf. Technol.* **96** 2791–801
- [79] Foster B K, Reutzel E W, Nassar A R, Hall B T, Brown S W and Dickman C J 2015 Optical, layerwise monitoring of powder bed fusion *Int. Solid Freeform Fabrication Symp.*
- [80] Keaveney S, Shmeliov A, Nicolosi V and Dowling D P 2020 Investigation of process by-products during the selective laser melting of Ti6Al4V powder *Addit. Manuf.* **36** 101514
- [81] Craeghs T, Clijsters S, Yasa E and Kruth J-P 2011 Online quality control of selective laser melting *SFF 2011* (available at: www.researchgate.net/publication/268293509)
- [82] Kleszczynski S, Seht J, Witt G and Zur Jacobsmühlen J 2012 Error detection in laser beam melting systems by high resolution imaging *Int. Solid Freeform Fabrication Symp.* (available at: www.lfb.rwth-aachen.de)
- [83] Zur Jacobsmühlen J, Kleszczynski S, Schneider D and Witt G 2013 High resolution imaging for inspection of laser beam melting systems *IEEE Int.*
- [84] Lu Q Y, Nguyen N V, Hum A J W, Tran T and Wong C H 2020 Identification and evaluation of defects in selective laser melted 316L stainless steel parts via in-situ monitoring and micro computed tomography *Addit. Manuf.* **35** 101287
- [85] Snow Z, Diehl B, Reutzel E W and Nassar A 2021 Toward in-situ flaw detection in laser powder bed fusion additive manufacturing through layerwise imagery and machine learning *J. Manuf. Syst.* **59** 12–26
- [86] Abdelrahman M, Reutzel E W, Nassar A R and Starr T L 2017 Flaw detection in powder bed fusion using optical imaging *Addit. Manuf.* **15** 1–11
- [87] Modaresialam M, Roozbahani H, Alizadeh M, Salminen A and Handroos H 2022 In-situ monitoring and defect detection of selective laser melting process and impact of process parameters on the quality of fabricated SS 316L *IEEE Access* **10** 46100–13
- [88] Fischer F G, Birk N, Rooney L, Jauer L and Schleifenbaum J H 2021 Optical process monitoring in laser powder bed fusion using a recoater-based line camera *Addit. Manuf.* **47** 102218
- [89] Aminzadeh M and Kurfess T R 2019 Online quality inspection using Bayesian classification in powder-bed additive manufacturing from high-resolution visual camera images *J. Intell. Manuf.* **30** 2505–23
- [90] Gobert C, Reutzel E W, Petrich J, Nassar A R and Phoha S 2018 Application of supervised machine learning for defect detection during metallic powder bed fusion additive manufacturing using high resolution imaging *Addit. Manuf.* **21** 517–28
- [91] Caltanissetta F, Grasso M, Petró S and Colosimo B M 2018 Characterization of in-situ measurements based on layerwise imaging in laser powder bed fusion *Addit. Manuf.* **24** 183–99
- [92] Zur Jacobsmühlen J, Kleszczynski S, Witt G and Merhof D 2016 Elevated region area measurement for quantitative analysis of laser beam melting process stability *Int. Solid Free Form Fabrication*
- [93] Boone N, Zhu C, Smith C, Todd I and Willmott J R 2018 Thermal near infrared monitoring system for electron beam melting with emissivity tracking *Addit. Manuf.* **22** 601–5
- [94] Cordero Z C, Dinwiddie R B, Immel D and Dehoff R R 2017 Nucleation and growth of chimney pores during electron-beam additive manufacturing *J. Mater. Sci.* **52** 3429–35
- [95] Raplee J, Plotkowski A, Kirka M M, Dinwiddie R, Okello A, Dehoff R R and Babu S S 2017 Thermographic microstructure monitoring in electron beam additive manufacturing *Sci. Rep.* **7** 43554
- [96] Krauss H, Zeugner T and Zaeh M F 2015 Thermographic process monitoring in powderbed based additive manufacturing *AIP Conf. Proc.* **1650** 177–83
- [97] Yoder S, Morgan S, Kinzy C, Barnes E, Kirka M, Paquit V, Nandwana P, Plotkowski A, Dehoff R R and Babu S S 2018 Characterization of topology optimized Ti-6Al-4V components using electron beam powder bed fusion *Addit. Manuf.* **19** 184–96
- [98] Schwerz C, Raza A, Lei X, Nyborg L, Hryha E and Wirdelius H 2021 In-situ detection of redeposited spatter and its influence on the formation of internal flaws in laser powder bed fusion *Addit. Manuf.* **47** 102370
- [99] Nandwana P, Kirka M M, Paquit V C, Yoder S and Dehoff R R 2018 Correlations between powder feedstock quality, in situ porosity detection, and fatigue behavior of Ti-6Al-4V fabricated by powder bed electron beam melting: a step towards qualification *JOM* **70** 1686–91
- [100] Mahmoudi M, Ezzat A A and Elwany A 2019 Layerwise anomaly detection in laser powder-bed fusion metal additive manufacturing *J. Manuf. Sci. Eng.* **141** 031002
- [101] Bartlett J L, Heim F M, Murty Y V and Li X 2018 In situ defect detection in selective laser melting via full-field infrared thermography *Addit. Manuf.* **24** 595–605
- [102] Yakout M, Phillips I, Elbestawi M A and Fang Q 2021 In-situ monitoring and detection of spatter agglomeration and delamination during laser-based powder bed fusion of Invar 36 *Opt. Laser Technol.* **136** 106741

- [103] Mireles J, Terrazas C, Gaytan S M, Roberson D A and Wicker R B 2015 Closed-loop automatic feedback control in electron beam melting *Int. J. Adv. Manuf. Technol.* **78** 1193–9
- [104] Schwerz C, Bircher B A, Küng A and Nyborg L 2023 In-situ detection of stochastic spatter-driven lack of fusion: application of optical tomography and validation via *ex-situ* x-ray computed tomography *Addit. Manuf.* **72** 103631
- [105] Bamberg J, Zenzinger G and Ladewig A 2016 In-process control of selective laser melting by quantitative optical tomography *World Conf. on Non-Destructive Testing* (available at: <http://creativecommons.org/licenses/by/3.0/>)
- [106] Arnold C, Pobel C, Osmanlic F and Körner C 2018 Layerwise monitoring of electron beam melting via backscatter electron detection *Rapid Prototyp. J.* **24** 1401–6
- [107] Wong H, Neary D, Jones E, Fox P and Sutcliffe C 2019 Pilot capability evaluation of a feedback electronic imaging system prototype for in-process monitoring in electron beam additive manufacturing *Int. J. Adv. Manuf. Technol.* **100** 707–20
- [108] Pobel C R, Arnold C, Osmanlic F, Fu Z and Körner C 2019 Immediate development of processing windows for selective electron beam melting using layerwise monitoring via backscattered electron detection *Mater. Lett.* **249** 70–72
- [109] Arnold C, Böhm J and Körner C 2020 In operando monitoring by analysis of backscattered electrons during electron beam melting *Adv. Eng. Mater.* **22** 1901102
- [110] Franke M, Arnold C and Körner C 2023 In-situ quality assurance for electron-based additive manufacturing by electron optical observation *Prog. Addit. Manuf.* **8** 55–60
- [111] Gardfjell M, Reith M, Franke M and Körner C 2023 In situ inclusion detection and material characterization in an electron beam powder bed fusion process using electron optical imaging *Materials* **16** 4220
- [112] Liu M, Senin N and Leach R 2021 Intelligent quality monitoring for additive manufactured surfaces by machine learning and light scattering *Proc. SPIE* **11782** 17–26
- [113] Land W S, Zhang B, Ziegert J and Davies A 2015 In-situ metrology system for laser powder bed fusion additive process *Proc. Manuf.* **1** 393–403
- [114] Kalms M, Narita R, Thomy C, Vollertsen F and Bergmann R B 2019 New approach to evaluate 3D laser printed parts in powder bed fusion-based additive manufacturing in-line within closed space *Addit. Manuf.* **26** 161–5
- [115] Zhang B, Ziegert J C, Land II W S, Ziegert J and Davies A 2015 In situ monitoring of laser powder bed fusion additive manufacturing using digital fringe projection technique *ASPE* (available at: www.researchgate.net/publication/283097423)
- [116] Zhang B, Ziegert J, Farahi F and Davies A 2016 In situ surface topography of laser powder bed fusion using fringe projection *Addit. Manuf.* **12** 100–7
- [117] Southon N, Stavroulakis P, Goodridge R and Leach R 2018 In-process measurement and monitoring of a polymer laser sintering powder bed with fringe projection *Mater. Des.* **157** 227–34
- [118] Dickins A, Widjanarko T, Sims-Waterhouse D, Thompson A, Lawes S, Senin N and Leach R 2020 Multi-view fringe projection system for surface topography measurement during metal powder bed fusion *J. Opt. Soc. Am. A* **37** B93
- [119] Remani A, Williams R, Thompson A, Dardis J, Jones N, Hooper P and Leach R Design of a multi-sensor measurement system for in-situ defect identification in metal additive manufacturing (available at: www.euspen.eu)
- [120] Neef A, Seyda V, Herzog D, Emmelmann C, Schönleber M and Kogel-Hollacher M 2014 Low coherence interferometry in selective laser melting *Phys. Proc.* **56** 82–89
- [121] DePond P J, Guss G, Ly S, Caltan N P, Deane D, Khairallah S and Matthews M J 2018 In situ measurements of layer roughness during laser powder bed fusion additive manufacturing using low coherence scanning interferometry *Mater. Des.* **154** 347–59
- [122] Fleming T G, Nestor S G L, Allen T R, Boukhaled M A, Smith N J and Fraser J M 2020 Tracking and controlling the morphology evolution of 3D powder-bed fusion in situ using inline coherent imaging *Addit. Manuf.* **32** 100978
- [123] de Groot P 2011 Coherence scanning interferometry *Optical Measurement of Surface Topography* ed R Leach (Springer) pp 187–208
- [124] Barrett C, MacDonald E, Conner B and Persi F 2018 Micron-level layer-wise surface profilometry to detect porosity defects in powder bed fusion of inconel 718 *JOM* **70** 1844–52
- [125] Tan Phuc L and Seita M 2019 A high-resolution and large field-of-view scanner for in-line characterization of powder bed defects during additive manufacturing *Mater. Des.* **164** 107562
- [126] Kouprianoff D, Yadroitsava I, du Plessis A, Luwes N and Yadroitsev I 2021 Monitoring of laser powder bed fusion by acoustic emission: investigation of single tracks and layers *Front. Mech. Eng.* **7** 678076
- [127] Pieris D *et al* 2019 Spatially resolved acoustic spectroscopy towards online inspection of additive manufacturing *Acoust. Spectrosc.* **61** 132–7
- [128] Peng X and Kong L 2022 Development of a multi-sensor system for defects detection in additive manufacturing *Opt. Express* **30** 30640
- [129] Petrich J, Snow Z, Corbin D and Reutzel E W 2021 Multi-modal sensor fusion with machine learning for data-driven process monitoring for additive manufacturing *Addit. Manuf.* **48** 102364
- [130] Snow Z, Reutzel E W and Petrich J 2022 Correlating in-situ sensor data to defect locations and part quality for additively manufactured parts using machine learning *J. Mater. Process. Technol.* **302** 117476